ROYAL SOCIETY OF CHEMISTRY

PAPER

Check for updates

High-performance polyimine xerogels: a lightweight and recyclable solution for high-temperature oil adsorption

Uyen Phuong Trieu,†[ab] Hoan Ngoc Doan, (ID) †[bc] Vy Tuong Thanh Nguyen,[ab] Trang Thu Thi Nguyen,[ab] Ha Tran Nguyen, (ID) [bde] Hieu Minh Doan,[bde] Ut Thach Dong (ID) [f] and Phu Phong Vo (ID) *[ab]

The remediation of viscous oil spills and organic contaminants in harsh environments requires sorbents that possess not only adsorption capability but also exceptional thermal and chemical stability. Herein, we report the facile synthesis of a novel class of fluorinated copolyimine xerogels (XG-CoPI) following the solvent exchange method *via* the polycondensation of terephthalaldehyde (PA), 4,4′-oxydianiline (ODA), and 2,2′-bis(trifluoromethyl)benzidine (6FAPB). To enhance the mechanical properties and thermal stability, the material was cross-linked using tris(2-aminoethyl)amine (TREN). The copolyimine xerogel with 10 wt% solid content (XG-CoPI10) exhibits an optimum porous xerogel structure with a low density of 0.229 g cm^{-3}, and exceptional thermal stability, exhibiting a decomposition temperature exceeding 300 °C. Notably, XG-CoPI10 achieved a superior hot-oil adsorption capacity of 3.83 g g^{-1} at 150 °C, which outperformed its room-temperature capacity (3.21 g g^{-1}). Furthermore, the xerogel demonstrated outstanding cyclic durability, maintaining a high adsorption efficiency over 10 high-temperature adsorption–desorption cycles. Additionally, it exhibited excellent chemical stability, with a mass retention exceeding 96% in organic solvents, including DMF and NMP. These quantitative results demonstrate XG-CoPI as a high-performance candidate for high-temperature oil spill remediation and industrial wastewater purification.

1. Introduction

Water scarcity and marine pollution represent two of the most pressing challenges confronting global sustainability in the 21st century. Despite covering more than 70% of the Earth's surface and serving as a critical regulator of planetary climate systems, oceanic ecosystems face escalating threats from intensified anthropogenic pressures. Among the diverse array of marine contaminants, oil spills - originating from offshore drilling operations, maritime transportation incidents, and industrial effluents - constitute a particularly severe hazard to both marine biodiversity and human welfare.[1–3] Oil film formation on water surfaces inhibits critical air-sea gas exchange and

photosynthetic processes, whilst facilitating the transfer of toxic hydrocarbons into marine food chains, leading to severe and persistent ecological and socioeconomic damage.[4,5] Consequently, developing rapid, efficient, and environmentally sustainable oil spill remediation technologies has become a global imperative.

In recent years, adsorption technology using porous materials has attracted significant attention as a superior alternative to traditional mechanical skimming or chemical dispersants.[6,7] Advanced porous materials, particularly aerogels or xerogels, have demonstrated exceptional oil sorption capacities due to their high porosity and low density.[8–10] However, the widespread industrial application of aerogels is severely hindered by energy-intensive fabrication processes, most notably supercritical CO_2 drying, and their intrinsic mechanical fragility, which compromises structural integrity during recovery and limits cyclic reusability.[10,11] In contrast, xerogels prepared *via* ambient pressure drying (APD) offer a cost-effective alternative that retains high porosity whilst circumventing these drawbacks.[12] The primary challenge in xerogel fabrication lies in overcoming strong capillary forces during solvent evaporation, which typically induce structural shrinkage and densification.[12,13] Therefore, constructing a robust chemical backbone capable of

[a]*Faculty of Chemistry, University of Science, Ho Chi Minh City, Vietnam. E-mail: vpphu@hcmus.edu.vn*

[b]*Viet Nam National University Ho Chi Minh City, Vietnam*

[c]*School of Biomedical Engineering, International University, Ho Chi Minh City, Vietnam*

[d]*Key Laboratory for Polymer and Composite Materials, Viet Nam National University Ho Chi Minh City, Vietnam*

[e]*Ho Chi Minh City University of Technology, Ho Chi Minh City, Vietnam*

[f]*Research Group in Pharmaceutical and Biomedical Sciences, Faculty of Pharmacy, Ton Duc Thang University, Ho Chi Minh City, Vietnam*

† These authors contributed equally to this work.

sustaining high porosity without relying on complex drying protocols remains a significant hurdle in materials science.

Among the adsorption xerogel materials, polyimines (PIs) are known as a potential material.[14–16] Compared to traditional polyimides, significant economic advantages are offered by polyimines. They are considered much more cost-effective to produce synthesis, polyimines are prepared more easily. Unlike polyimines, the imidization step at high temperature is required for the formation of polyimide. PIs can be synthesized without using high temperatures, making the synthesis process very convenient. To adapt PIs for oil spill remediation, the chemical structure must be meticulously designed to maximize hydrophobicity and oleophilicity. Recent studies suggest that incorporating fluorinated moieties (such as –CF$_3$ groups) into the polymer backbone can significantly lower surface energy, thereby enhancing water repellency and stabilizing the porous structure against capillary stress during ambient drying.[17] Furthermore, the introduction of aromatic rings facilitates strong π–π stacking interactions with oil molecules, increasing the adsorption capacity.[9] Besides xerogel materials, nanocomposites and nanomaterials have been widely developed for environmental remediation in recent years. Among the various fabrication approaches, the sol–gel method has been widely employed for the synthesis of nano-mesoparticles and supramolecular metallogels, owing to its low processing temperature,

controllable porosity.[18,19] The resulting ceramic materials and metal oxide nanoparticles are frequently utilized as inorganic fillers in the production of polymer-based nanocomposites.[20] The fabrication method of these materials typically involves blending nanofillers into a polymer matrix. However, this multi-step fabrication presents significant challenges. The inorganic fillers tend to agglomerate within the polymer matrix, leading to poor dispersion and compromised material performance.

Addressing these challenges, this work reports the facile synthesis of a novel hydrophobic copolyimine *via* a catalyst-free sol–gel process. The copolyimine xerogel was formed following by solvent exchange and an ambient pressure drying method. Specifically, *p*-phthalaldehyde (PA) was reacted with a combination of two diamines. To provide structural rigidity, 4,4-diaminodiphenyl ether (4,4-ODA) was utilized. Besides that, a fluorinated monomer, 4-bis(4-amino-2-trifluoromethylphenoxy) benzene 6FAPB, was incorporated to increase the superhydrophobicity of the PIs. Furthermore, to enhance the chemical stability, tris(2-aminoethyl) amine (TREN) was employed as a trifunctional crosslinker. By optimizing the solid content and utilizing a simple solvent exchange process from *N*-methyl-2-pyrrolidone (NMP) to ethanol, we successfully fabricated xerogels that retain high porosity and exhibit superior hydrophobicity. This work investigated the structural properties, thermal properties,
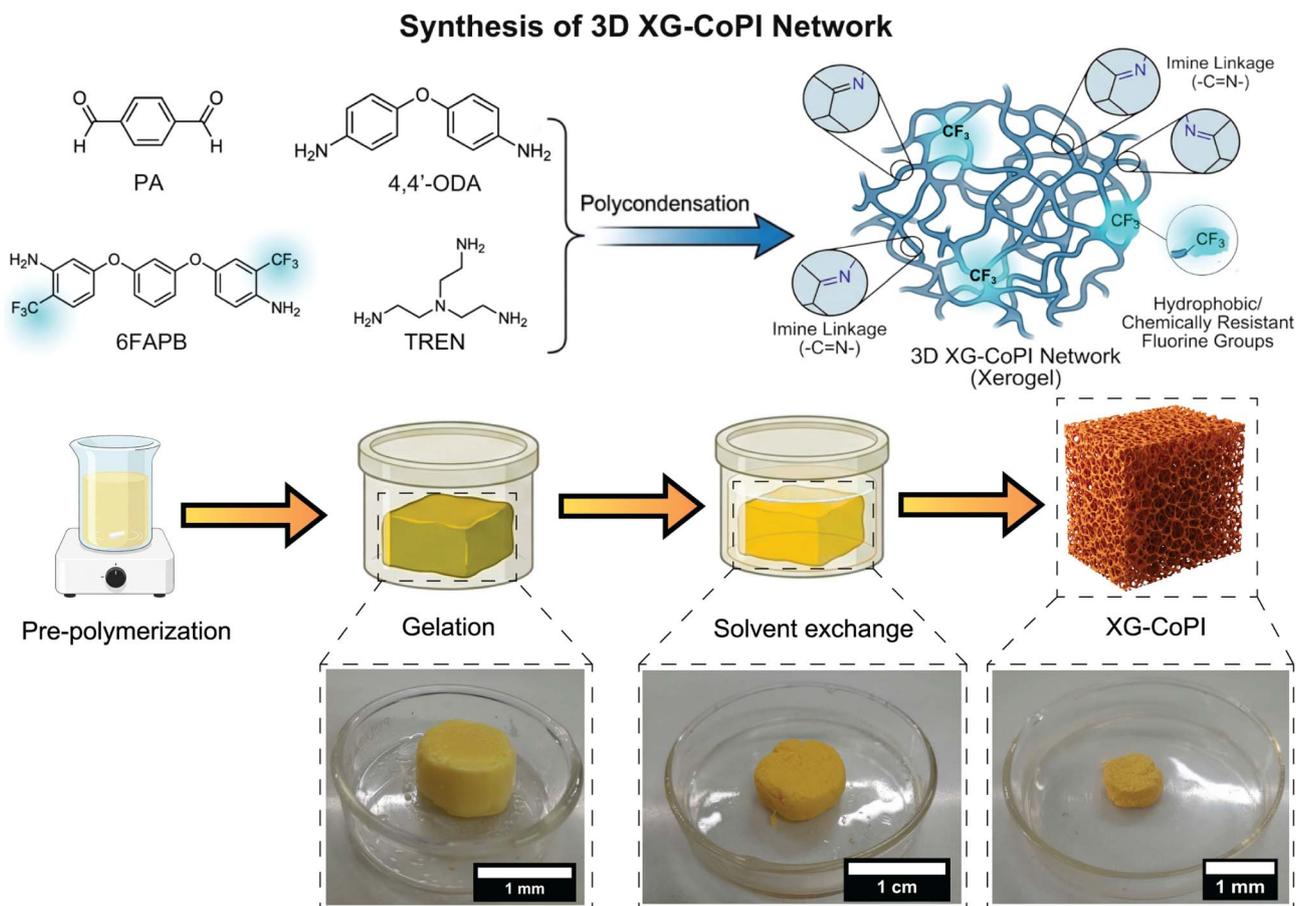

Fig. 1 The synthesis process of XG-CoPI *via* the solvent exchange process.

mechanical stability, and oil sorption performance of copolyimine xerogels, offering a scalable, cost-effective, and reusable solution for advanced oil spill remediation.

2. Experimental section

2.1. Materials

p-Phthalaldehyde (PA, 98%), 1,4-bis(4-amino-2-trifluoromethylphenoxy)benzene (6FAPB, ≥98%), tris(2-aminoethyl)amine (TREN, 97%), and 4,4′-diaminodiphenyl ether (4,4′-ODA, 98%) were sourced from Macklin (China). *N*-methyl-2-pyrrolidone (NMP, ≥99.7%) was supplied by Fisher Chemical (USA). Ethanol (EtOH, 99.5%), *N, N*-dimethylformamide (DMF, 99.5%), and acetone (99.5%) were obtained from Xilong (China). All reagents were used as received without further purification.

2.2. Synthesis of the copolyimine xerogels (XG-CoPI)

Copolyimine xerogels (XG-CoPI) were synthesised *via* a room temperature Schiff-base polycondensation between PA, 4,4′-ODA, 6FAPB, and TREN in a molar ratio of 12 : 3 : 3 : 4, respectively. A schematic representation of the synthesis and gel preparation process is illustrated in Fig. 1a.

In a typical procedure, two separate solutions were prepared. First, a solution of PA was prepared in 20 mL vial by dissolving the required amount of PA in 2.000 g of NMP. In a separate vial, a mixture of 4,4′-ODA, 6FAPB, and TREN was dissolved in 3.000 g of NMP with magnetic stirring until a homogeneous solution was formed. The PA solution was then added dropwise to the stirred amine solution at room temperature. The resulting mixture solution was stirred at 300 rpm until a homogeneous, viscous solution was obtained. This procedure was repeated to prepare a series of four solutions with various final solid contents of 5, 7.5, 10, and 12.5 wt%. The precise masses of each reagent used for the different formulations are detailed in Table 1.

For gelation process, the resulting solution was cast into a mold and left undisturbed at ambient temperature for 24 h to complete the gelation process.[8] This process resulted in the formation of a stable, yellow-translucent wet gel, as shown in Fig. 1b. To remove the residual high-boiling point solvent, the as-prepared wet gel was subjected to a systematic solvent exchange procedure. The gel was immersed in a mixture of ethanol (EtOH) and NMP. The solvent mixture was replaced at

Table 1 The monomer composition of XG-CoPI with various solid contents

Sample	Monomer composition				
	PA (g)	4,4′-ODA (g)	6FAPB (g)	TREN (g)	NMP (g)
XG-CoPI5	0.099	0.037	0.079	0.036	5.000
XG-CoPI7.5	0.147	0.05	0.118	0.054	5.000
XG-CoPI10	0.197	0.074	0.157	0.072	5.000
XG-CoPI12.5	0.247	0.092	0.197	0.090	5.000

Table 2 The composition of the solvent mixture was used for the solvent exchange process

Mixture solvent	Volume of solvent	
	NMP (ml)	EtOH (ml)
75 : 25	37.50	12.50
50 : 50	25.00	25.00
25 : 75	12.50	37.50
0 : 100[a]	0.00	50.00

[a] The step was repeated twice to ensure the complete removal of the NMP solvent.

2 h intervals for a total of 10 h. The appearance of the gel after the completion of the solvent exchange is depicted in Fig. 1c. The wet gels were dried at 70 °C, at ambient pressure for 24 h to obtain the final xerogels. The detailed solvent exchange protocol is summarized in Table 2.[21]

2.3. Characterization

The surface morphology and microstructure of the synthesized materials were investigated using Scanning Electron Microscopy (SEM) on a JSM-IT200 (JEOL Co., Ltd, Japan). The samples were coated with a thin layer of platinum prior to imaging to enhance conductivity. Attenuated Total Reflectance Fourier Transform Infrared (ATR-FT-IR) spectroscopy was employed to identify the chemical structures and functional groups of the samples. The spectra were recorded using spectrum two spectrometer (PerkinElmer Co., Ltd, US) in the wavenumber range of 4000–400 cm^{-1}. The mechanical properties were evaluated by measuring the compressive strength using a universal testing machine (Yang Yi Technology Co., Ltd, Taiwan) at a crosshead speed of 1 mm min^{-1}. Sections of the samples were cut into the cubic with a size 10*10*10 mm. The compressive strength (σ) was calculated using eqn (1)

$$\sigma(\text{MPa}) = \frac{F_{\max}}{A} \quad (1)$$

where $F_{\max}$ (N) is the maximum load applied to the sample, and A (mm^2) is the cross-sectional area.

The ρ (bulk density) of the samples was determined by measuring the weight and physical dimensions of the cubic specimens. The density was calculated according to eqn (2)

$$\rho = \frac{m}{V} \quad (2)$$

where m (g) is the mass of the sample in air, and V (cm^3) is the volume of the sample.

The heat resistance index of the sample was determined from the TGA analysis by the temperature at weight loss of 5% and 30%. The heat resistance index was calculated using eqn (3):

$$T_{\text{HRI}} = 0.49 \times [T_5 + 0.6 \times (T_{30} - T_5)] \quad (3)$$

where T_{HRI} is the heat resistance index, T_5 is the temperature corresponding to 5% weight loss, T_{30} is the temperature corresponding to 30% weight loss.

2.4. Oil adsorption capacity

The oil adsorption capacity was determined using a static immersion method. The pre-weighed samples were immersed in 20 mL of vegetable oil at room temperature and 150 °C. At specific time intervals, the samples were removed, allowed to drain for 10 seconds to remove excess surface oil, and weighed. The adsorption capacity was calculated using eqn (4):

$$W \left(g\ g^{-1}\right) = \frac{m_a - m_o}{m_o} \qquad (4)$$

where W is adsorption capacity, m_o is pre-weigh samples, m_a is the weight of the sample at the specific time intervals.

The reusable ability of XG-CoPI was evaluated using a centrifugal removal method.[22] The sample after immersion in 20 mL of vegetable oil was centrifuged in 5 min at 2000 rpm to remove the excess oil. This process was repeated 10 times. For each circle, the adsorption capacity was calculated following the eqn (5)

$$W_{\text{oil desorption}} \left(g\ g^{-1}\right) = \frac{m_1 - m_{\text{oil desorption}}}{m_0} \qquad (5)$$

where m_1 is the weight of sample after immersed in vegetable oil, $m_{\text{oil desorption}}$ is the weight of the sample after centrifuge, m_0 is the weight of the sample before immersed on vegetable oil.

2.5. Chemical stability

The solvent resistance of the XG-CoPI samples was assessed to evaluate their chemical stability. The dried CO-PI xerogels were weighed and immersed in 10 mL of various solvents, including N-methyl-2-pyrrolidone (NMP), N, N-dimethylformamide (DMF), and acetone, for 24 h at room temperature without stirring. Subsequently, the samples were removed, surface-
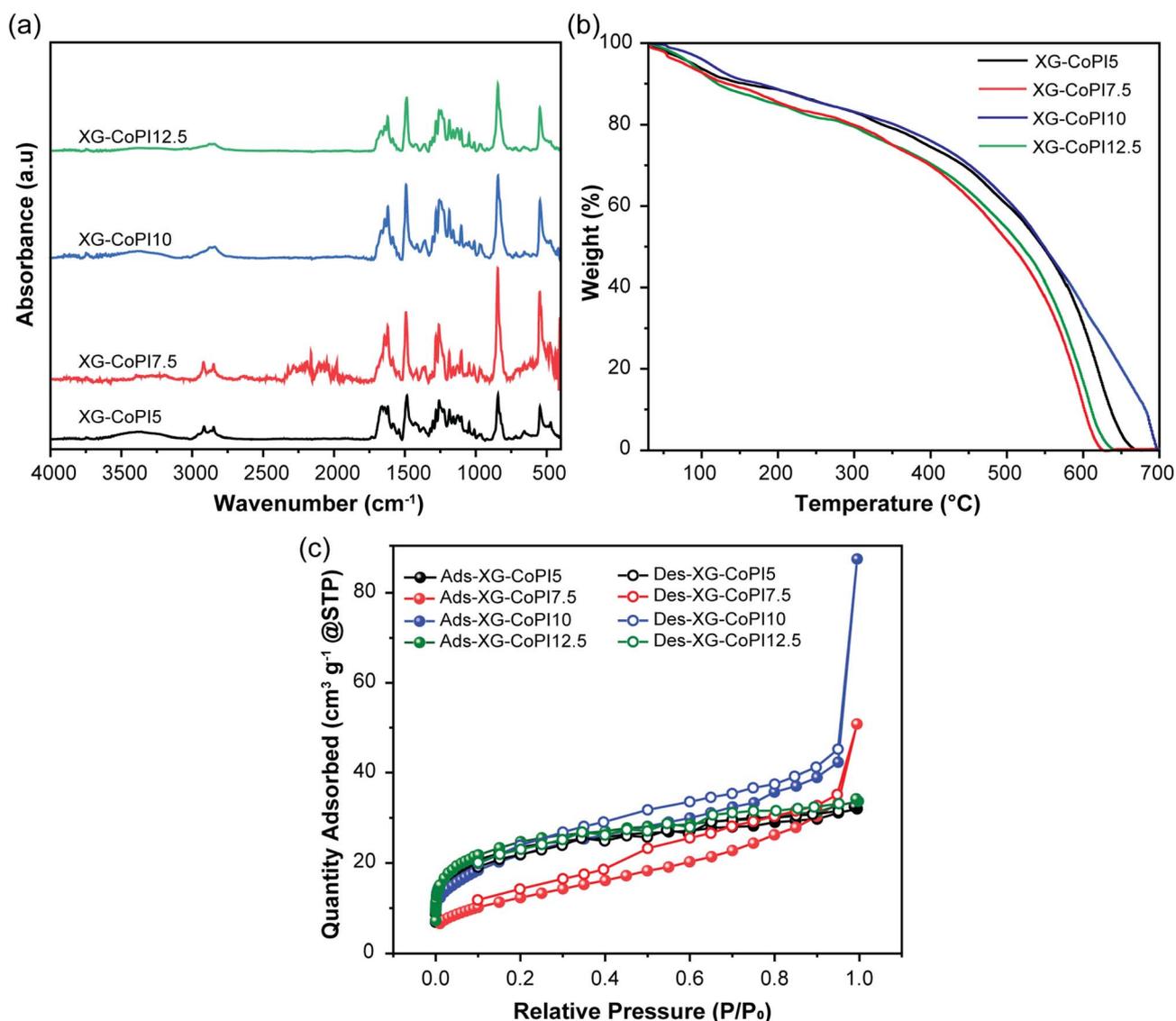

Fig. 2 (a) ATR-FTIR spectra of the XG-CoPI, (b) TGA curves of the XG-CoPI, (c) nitrogen adsorption–desorption isotherms curves of various solid contents.

dried, and heated at 50 °C until a constant weight was achieved. The weight retention was calculated using eqn (5).

$$W_{\text{retention}} \ (\%) = \frac{m_1}{m_0} \times 100 \qquad (6)$$

where $W_{\text{retention}}$ is weight retention, m_0 is the weight of the sample and m_1 is the weight of the sample after immersed in solvent.

3. Results and discussion

3.1. Formation of the fluorinated XG-CoPI network and thermal properties

As shown in Fig. 1, the fluorinated XG-CoPI xerogels were synthesized *via* a sol–gel process driven by Schiff-base polycondensation. The resulting material features a crosslinked aromatic polyimine network.[23] The FT-IR spectroscopy was employed to investigate the chemical structure of XG-CoPI prepared with varying solid contents. The ATR FT-IR spectrum of the XG-CoPI xerogels is presented in Fig. 2a. All samples exhibited nearly identical spectral profiles irrespective of initial monomer concentration, demonstrating that solid content variation does not affect the fundamental chemical composition of the polymer network.

The successful formation of the polyimine backbone is confirmed by the characteristic imine (–C=N) stretching vibration at 1624 cm^{-1}.[15,24] The Schiff-base reaction was verified by comparing the spectra with the pristine monomers (Fig. S1). Specifically, the aldehyde (C=O) band at 1690 cm^{-1} assigned to the PA monomer disappeared completely.[25]

Furthermore, the fluorinated groups remain consistent across all samples. Characteristic absorption bands at 1047 cm^{-1} and 1619 cm^{-1} correspond to C–F stretching of the 6FAPB moiety and aromatic skeletal vibrations, respectively.[17] The retention of these peaks across all solid contents confirms uniform incorporation of hydrophobic fluorinated groups and rigid aromatic segments into the xerogel framework. The chemical structure of Co-PI xerogels is promising for subsequent thermal and high-temperature adsorption applications.

Besides that, the thermal stability was evaluated, as it is a fundamental requirement for oil sorbents in high-temperature applications. Fig. 2b shows the thermogravimetric analysis (TGA) curve under nitrogen atmosphere. As shown in Fig. 2b, uniform thermal stability characteristics were observed for XG-CoPI across various solid contents. The TGA curves exhibited a two-stage weight loss behavior typical of porous polymeric networks. The first stage exhibits a minor

Table 3 The heat resistance index of XG-CoPI samples

Sample	T_5 (°C)	T_{30} (°C)	T_{HRI} (°C)
XG-CoPI5	92.0	443.0	148.3
XG-CoPI7.5	78.0	396.0	131.7
XG-CoPI10	112.0	451.0	154.5
XG-CoPI12.5	83.0	402.0	134.5

weight loss of approximately 5% commencing at 89 °C, attributed to desorption of physiosorbed moisture or residual solvent trapped within the mesopores.[26] Notably, after the initial solvent loss, the material displayed high thermal stability with negligible weight loss up to 200 °C. The second stage weight loss, corresponding to intrinsic thermal decomposition of the polymer backbone, does not commence until 500 °C. Besides that, the heat resistance index of the XG-CoPI was calculated and shown in Table 3.

As shown in Table 3, the thermal stability decreased for XG-CoPI7.5. This sample showed the lowest values, with a T_5 of 78.0 °C and a T_{HRI} of 131.7 °C. However, the performance increased significantly for XG-CoPI10. This sample exhibited the highest thermal stability. It reached a T_{30} of 451.0 °C and a peak T_{HRI} of 154.5 °C. However, the heat resistance index decrease again for XG-CoPI12.5. The variation of T_{HRI} that the monomer content significantly influenced the thermal stability. This exceptional thermal resistance significantly surpasses that of many conventional Schiff-base polymers and non-fluorinated polyimines. The outstanding stability arises from synergistic structural features: (i) extensive π-conjugation between electron-rich benzene rings and imine linkages, which lowers the internal energy and stabilizes C=N bonds against thermal cleavage;[27] (ii) high crosslinking density imparted by the tripodal TREN monomer, which restricts segmental chain motion;[28,29] and (iii) strong C–F bonds (bond energy ≈ 485 kJ mol^{-1}) from the 6FAPB moieties, which provide additional resistance to thermal dissociation.[30]

To investigate the porous structure, N$_2$ adsorption–desorption isotherms were recorded to quantify the structure of the XG-CoPI xerogels following the BET method. As shown on Fig. 2c, all samples exhibit characteristic Type IV isotherms with distinct H3-type hysteresis loops in the relative pressure range of $P/P_0 \sim 0.45$–1.0.[31] According to IUPAC classification, this profile provides strong evidence of a mesoporous architecture composed of slit-shaped pores, formed by the aggregation of sheet-like polymer particles.[32,33]

The porous structure parameters derived from N$_2$ adsorption–desorption isotherms are summarized in Table 4. The porosity evolution reveals a non-monotonic dependence on the solid content. This trend highlights a trade-off between specific surface area (S_{BET}) and accessible pore volume (V_{total}). While XG-CoPI12.5 exhibits the highest S_{BET} of 86.1 m^2 g^{-1}. However, its total pore volume is significantly low at 0.053 cm^3 g^{-1}. This is attributed to the excessive formation of micropores (V_{micro} ∼0.021 cm^3 g^{-1}), which likely results from the dense interpenetration of polymer chains at high monomer concentrations. In contrast, XG-CoPI10 demonstrates the most optimized porous structure for oil adsorption application. It achieves the highest total pore volume of 0.135 cm^3 g^{-1}. Furthermore, this sample features a dominant mesoporosity of 97.3%.

This structural optimization in XG-CoPI10 can be attributed to the suitability of the solid content. At 10 wt%, the structure is sufficiently rigid to resist capillary collapse during solvent evaporation. In contrast, the XG-CoPI7.5 suffered a significant loss in porosity (S_{BET} = 44.7 m^2 g^{-1}). This result can be explained by the deformation of the structure during the drying

Table 4 Porous characteristics of XG–CoPI samples

Sample	S_{BET} (m² g⁻¹)	V_{micro} (cm³ g⁻¹)	V_{STP} (cm³ g⁻¹)	V_{total} (cm³ g⁻¹)	V_{meso} (cm³ g⁻¹)	Mesopore (%)
XG-CoPI5	84.0	0.0119	32.01	0.0495	0.0376	76.0%
XG-CoPI7.5	44.7	0.0024	50.83	0.0786	0.0762	96.9%
XG-CoPI10	78.5	0.0036	87.53	0.1354	0.1318	97.3%
XG-CoPI12.5	86.1	0.0209	34.23	0.0530	0.0321	60.6%

process. Conversely, avoiding the over solid content effect seen in XG-CoPI12.5 allows XG-CoPI10 to preserve large mesoporous structure. XG-CoPI10 has a slightly lower specific surface area than XG-CoPI12.5. However, the increase in mesoporous volume provides a larger reservoir for oil molecules. This structural advantage minimizes diffusion resistance and maximizes oil adsorption capacity. The porous structure characteristics demonstrated by BET analysis exhibited well-developed porous architecture, confirming the potential of XG-CoPI as a high-performance material for hot-oil adsorption.

3.2. Morphology and density

The influence of solid content on the microstructural evolution of XG-CoPI xerogels was investigated using scanning electron microscopy (SEM) and bulk density measurements. Understanding this relationship is crucial for optimizing the porous architecture required for efficient oil adsorption.

Fig. 3a–d shows the SEM images of various XG-CoPI with different solid content. A characteristic three-dimensional porous network was observed for all samples *via* SEM images. This structure is composed of irregularly shaped micro-sheets and interconnected particles with notably rough surfaces. This morphology is conducive to an enhanced specific surface area. However, the degree of porosity and structural uniformity varies significantly with the initial monomer concentration. This variation reflects a delicate balance between network formation kinetics and capillary-driven densification during solvent evaporation.[8]

As shown in Fig. 3a–b, at low solid contents (5% and 7.5 wt%), the XG-CoPI shows a relatively collapsed and dense morphology with diminished surface roughness. XG-CoPI-5 exhibits localized regions of dense agglomeration. This observation is indicative of inhomogeneous gelation in a dilute solution. Under these conditions, the polymer chain distribution is non-uniform. The resulting weak structure does not have sufficient mechanical rigidity to withstand capillary forces generated during solvent removal, leading to severe structural shrinkage and pore collapse.[34,35] This morphological observation is quantitatively corroborated by bulk density measurements. Fig. 3e shown the density of various XG-CoPI sample. The XG-CoPI-5 exhibits the highest density of 0.361 ± 0.013 g cm⁻³. This result arises from extensive volume
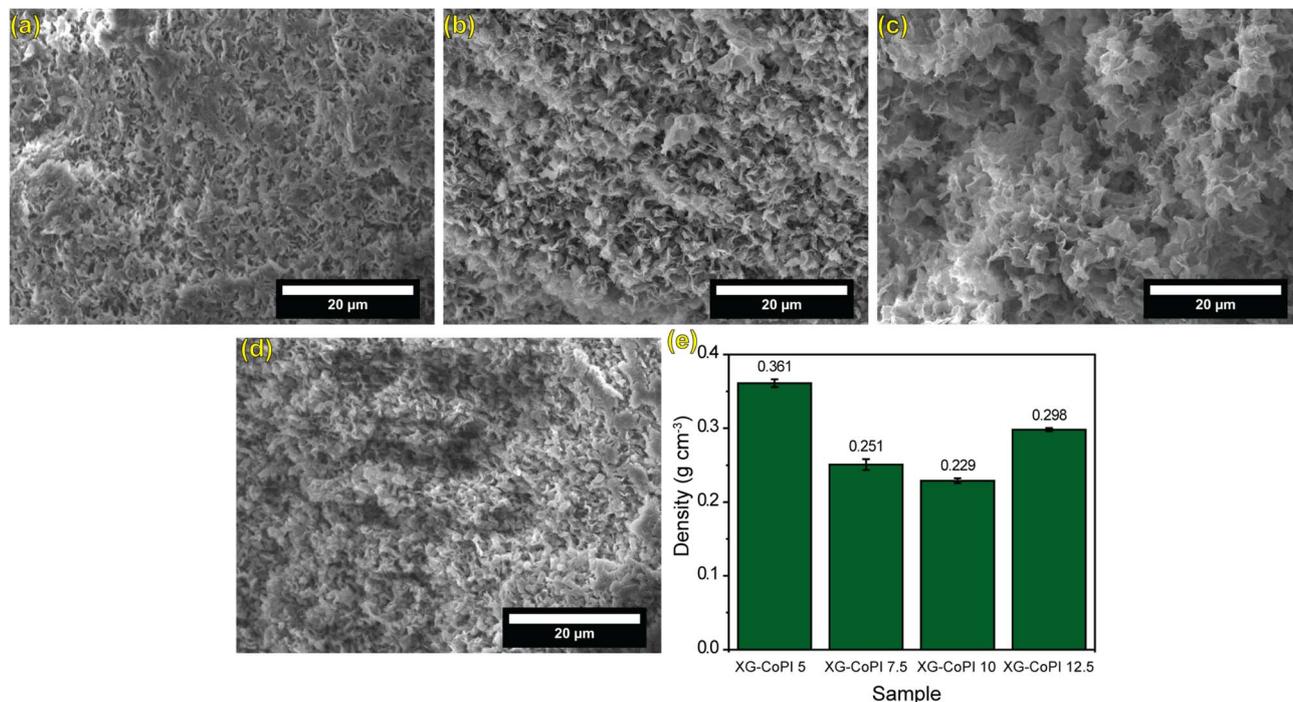

Fig. 3 The SEM images of the XG–CoPI sample with various solid contents: (a) 5%, (b) 7.5%, (c) 10%, (d) 12.5%, and (e) density of the prepared xerogel samples.

contraction induced by capillary stress in a mechanically weak network.[21]

A distinct morphological transformation occurs at the optimal solid content of 10 wt%. XG-CoPI-10 exhibited the most developed porous structure, as shown in Fig. 3c. This morphology is characterized by loose stacks of thin sheets. These sheets feature highly roughened surfaces and abundant interstitial voids. At this concentration, the solid content is sufficient to form a robust network. This structure effectively resists capillary-induced shrinkage. Furthermore, the concentration is not excessive, which prevents the dense packing of polymer chains. Consequently, XG-CoPI-10 exhibits the lowest bulk density of 0.229 ± 0.008 g cm^{-3}. This value corresponds to the most expanded and porous structure among all samples. Further increasing the solid content to 12.5 wt% results in a denser morphology, as shown in Fig. 3d, but porous structure of the XG-CoPI-12.5 is retained. However, the pore size is reduced significantly. This reduction is caused by the excessive monomer concentration. Such high concentration promotes the tight packing and interpenetration of polymer chains leading to occupies free volume of polymer chains and partially blocks mesoporous channels.[36] This effect is evidenced by a moderate increase in bulk density to 0.298 ± 0.005 g cm^{-3}. Notably, this density elevation arises from intrinsic matrix densification rather than capillary-driven collapse.

The non-linear density trend reflects the competition between two mechanisms. At low concentrations, capillary-induced collapse is dominant. In contrast, at high concentrations, the microstructure is mainly driven by the polymer-rich phase. The convergence of morphology and density analyses confirms that 10 wt% is the optimal solid content. This concentration maximizes porosity by effectively mitigating structural collapse and preventing dense polymer chain packing. Consequently, this optimized architecture establishes the foundation for superior oil adsorption performance, as discussed in the next section.

3.3. Oil adsorption

Experimental kinetic data were fitted to pseudo-first-order (PFO) and pseudo-second-order (PSO) models. This analysis aims to investigated the adsorption mechanism and identify the rate-controlling steps. The linearized plots are presented in Fig. 4a. Corresponding parameters are summarized in Table 5. The plots of t/q_t *versus* t exhibit excellent linearity across all samples, providing preliminary evidence for PSO kinetics. This is quantitatively confirmed by the correlation coefficients (R^2), which consistently exceed 0.99 for the PSO model while remaining substantially lower for the PFO model. For the optimal XG-CoPI10 sample, the PSO model yields $R^2 = 0.9973$ compared to 0.9902 for PFO, demonstrating superior statistical fit. More critically, the calculated equilibrium adsorption capacity (q_e, cal) from the PSO model (3.77 g g^{-1}) shows excellent agreement with the experimental value (q_e, exp = 3.83 g g^{-1}), with a relative deviation of merely 1.6%. In contrast, the PFO model severely underestimates the capacity (1.05 g g^{-1}), yielding a 72.6% deviation that disqualifies its applicability to this system.

The experimental data exhibits a high conformity to the pseudo-second-order kinetic model. This suggests that the adsorption is a surface-reaction-controlled process. Therefore, the rate-limiting step is dominated by surface interactions rather than physical diffusion.[37,38] This mechanism is attributed to the chemical functionalities of the XG-CoPI framework. Specifically, the framework contains electron-deficient fluorinated moieties (–CF$_3$ groups from 6FAPB) and conjugated imine linkages (–C=N–). These groups facilitate strong electron donor–acceptor complexation and π–π stacking interactions with aromatic hydrocarbons. Specific chemical interactions determine the adsorption rate, which sets XG-CoPI apart from standard materials driven by physisorption.

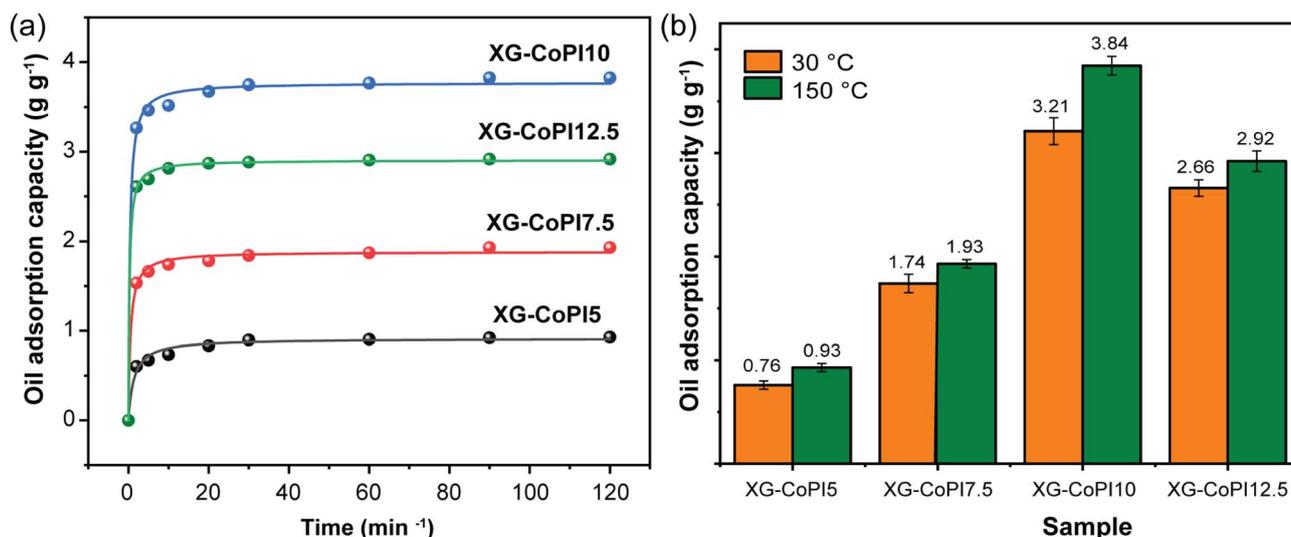Following the kinetic study, the thermal stability of the adsorbent was evaluated at elevated temperatures. This

Fig. 4 (a) The oil adsorption kinetics of XG-CoPI samples at 150 °C followed the pseudo-second-order model, (b) the maximum vegetable oil sorption capacities of the XG-CoPI at 30 °C and 150 °C.

Table 5 The kinetic parameters for oil adsorption on XG-CoPI xerogels at 150 °C

Sample	$q_{e,exp}$ (g g^{-1})	Pseudo-first-order model k_1 (min^{-1})	$q_{e, cal}$ (g g^{-1})	R^2	Pseudo-second-order model k_2 (g g^{-1} min^{-1})	$q_{e, cal}$ (g g^{-1})	R^2
XG-CoPI5	0.93	0.4641	0.86	0.9374	0.8045	0.91	0.9818
XG-CoPI7.5	1.93	0.8675	1.83	0.9822	1.0105	1.88	0.9950
XG-CoPI10	3.83	1.0522	3.70	0.9902	0.7487	3.77	0.9973
XG-CoPI12.5	2.92	1.1941	2.86	0.9948	1.3316	2.91	0.9990

property is critical for applications such as hot crude oil recovery and industrial wastewater treatment. Fig. 4b compares the saturated adsorption capacities at room and high temperature. As shown in Fig. 4b, all XG-CoPI xerogels retain the initial adsorption performance even at 150 °C. The maximum oil sorption capacity reached 3.21 g g^{-1}, and 3.84 g g^{-1} for XG-CoPI10 at 30 °C and 150 °C, respectively. This contrasts significantly with traditional absorbance materials, which typically undergo thermal deformation and pore closure at high temperatures. For XG-CoPI10, the capacity retention at high temperature is attributed to two synergistic factors. First, the high thermal stability, substantiated by thermogravimetric analysis, preserves the integrity of the pore structure.[39] Second, the elevated temperature substantially reduces oil viscosity, which lowers the activation energy for molecular diffusion. As a result, oil molecules can penetrate smaller mesopores and micropores that represent kinetically inaccessible sites at ambient temperature. This temperature-enhanced diffusion effectively offsets any potential capacity loss induced by thermal stress, resulting in sustained or even improved uptake performance.

3.4. Chemical stability and reusability

The practical applicability of porous sorbents in actual application not only on high adsorption capacity but also on exceptional chemical and mechanical stability, as well as long-term reusability. To investigate these attributes, the XG-CoPI xerogels were systematically evaluated through solvent immersion tests, mechanical compression testing, and cyclic reuse studies.

The chemical resistance of the fabricated xerogels was first evaluated by immersing the samples in three organic solvents of varying polarity—N-methyl-2-pyrrolidone (NMP), N,N-dimethylformamide (DMF), and acetone for 24 hours at ambient temperature. Fig. 5a showed the photograph of the xerogel samples immersed in the solvents for various time intervals. After the 24 h immersion in various solvents, the XG-CoPI samples exhibited dimensional stability, maintaining their original morphology. Visual inspection revealed that all immersion solvents remained transparent and colorless, indicating negligible leaching of unreacted monomers or oligomeric species. The weight retention of the XG-CoPI xerogels is presented in Fig. 5b. As shown in Fig. 5b, the weight retention analysis quantitatively corroborated the observation in Fig. 5a, with all samples preserving more than 86% of their initial mass across all immersion solvents. This exceptional chemical stability originates from the robust aromatic polyimine

backbone formed through the condensation of 4,4′-oxydianiline (ODA) and 6FAPB. The trifluoromethyl (–CF$_3$) groups incorporated from 6FAPB characterized by the high electronegativity of fluorine, significantly reduce the surface energy of the polymer network. This results in a significantly low surface energy state, effectively minimizing the interaction between the polymer backbone and immersion solvents. The XG-CoPI12.5 exhibited the highest solvent resistance (retention >96%), attributed to high density that physically restricts solvent diffusion. On the other hand, XG-CoPI7.5 exhibited the lowest weight retention of approximately 86–89% after immer 24 h. This observation corresponds to the porous structure, which allows for easier solvent diffusion. Notably, XG-CoPI5 exhibited higher stability when compared with XG-CoPI7.5. This phenomenon is attributed to the structural collapse observed via SEM images in Fig. 3a. This creates a dense layer that acts as a barrier to solvent diffusion.[21] The XG-CoPI10 sample exhibited excellent chemical durability. Specifically, the material retained over 89% of its mass in DMF and exceeded 95% in both NMP and acetone. Furthermore, the XG-CoPI10 maintained its porous structure. This stability indicates a good balance between porosity and chemical stability. Therefore, XG-CoPI10 is highly suitable for practical adsorption applications.

In addition to chemical stability, the mechanical properties of XG-CoPI were also investigated. They are significant for practical oil recovery application utilizing centrifugal force to release the absorbed oil. The compression stress–strain curve of prepared samples is shown in Fig. 5c. All samples demonstrated characteristic porous material behavior, defined by an initial linear elastic region and a subsequent densification region at high strain. XG-CoPI12.5 achieved the highest compressive stress of 77.68 MPa at 80% strain, which is attributed to the highly dense structure resulting from the high initial solid content. Besides that, XG-CoPI5 achieved the second-highest compressive stress of 40.97 MPa, greater than both XG-CoPI7.5 and XG-CoPI10 The higher compressive strength of XG-CoPI5 is attributed to structural shrinkage during the preparation process, which resulted in significantly reduced porosity. XG-CoPI10 exhibited an optimal balance of mechanical properties, achieving a compressive strength of 35.50 MPa at 80% strain. This is significantly higher than the 14.41 MPa of XG-CoPI7.5, while it still maintains a porous structure. These mechanical properties indicate that at a 10 wt% solid content, the polyimine molecules are interconnected to form a rigid structure. Consequently, this structure effectively resists shrinkage during the solvent exchange process.
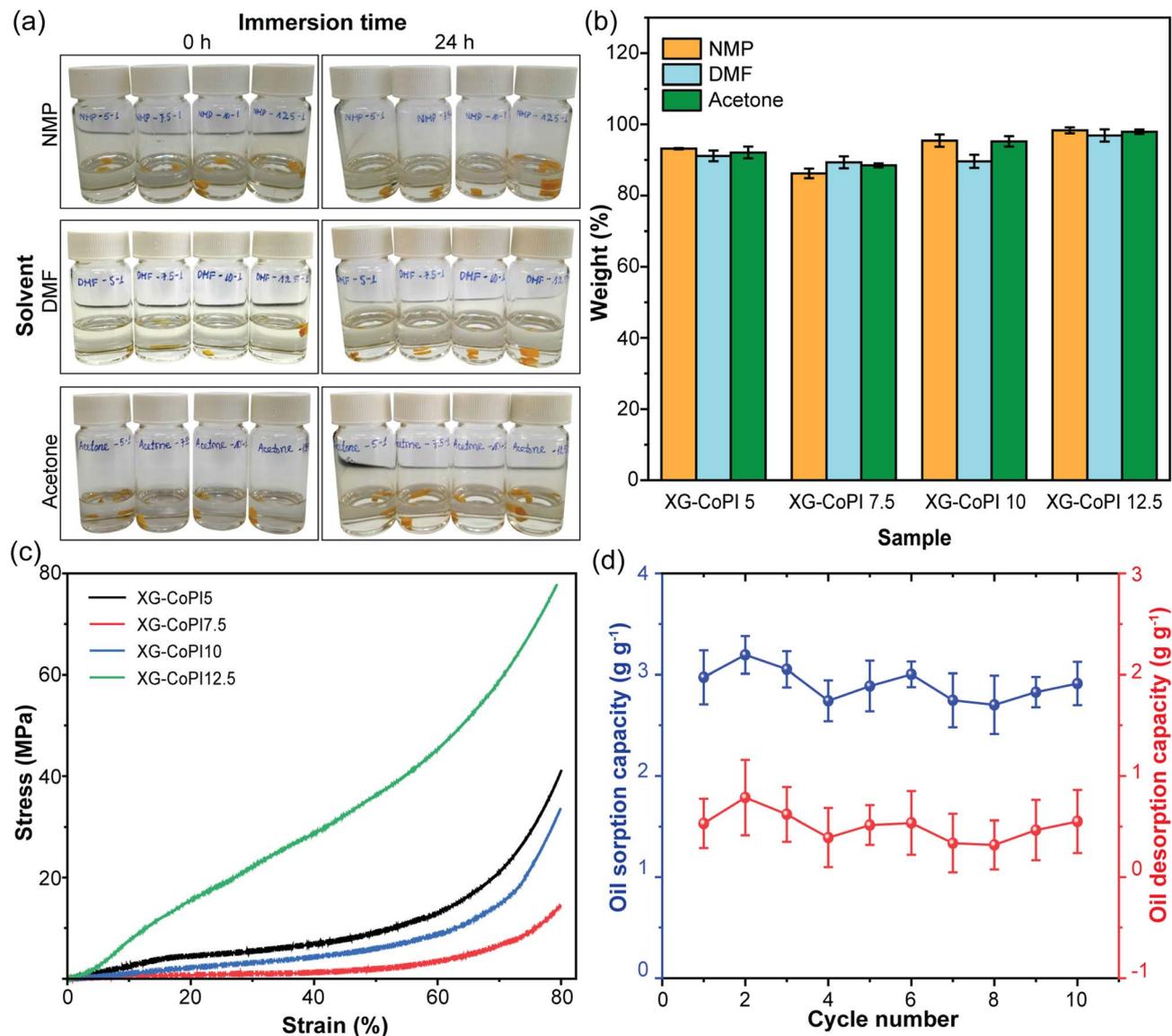
Fig. 5 (a) The photograph of the XG-CoPI10, (b) the weight retention of the XG-CoPI with various solid content after immersed 24 h in various solvent, (c) the stress–strain curve of the XG-CoPI with various solid content, (d) the oil sorption and oil desorption capabilities of the XG-CoPI10 after 10 cycles.

XG-CoPI exhibits superior mechanical properties, thereby enabling it to withstand centrifugal forces during the oil desorption process without structural deformation. As a result, the XG-CoPI demonstrates excellent reusability. This durability ensures the cost-effectiveness of XG-CoPI in industrial-scale oil removal applications. The reusability of XG-CoPI10 was evaluated through 10 adsorption–desorption cycles is shown in Fig. 5d, the material demonstrated outstanding reusability, maintaining a consistent oil sorption capacity in the range of 2.7–3.2 g g^{-1} with no significant performance attenuation over 10 successive cycles. The material maintained an adsorption capacity of 2.91 g g^{-1} after 10 cycles, exhibiting a minimal reduction from the initial 2.97 g g^{-1} and achieving retention rate of 98%. Furthermore, the amount of oil recovered via centrifugal force reached 0.55 g g^{-1} by the 10th cycle,

representing no significant decrease relative to the initial cycles. That result indicated the porous structure was not damaged after 10 adsorption–desorption cycles. These results demonstrate that the highly crosslinked polyimine network effectively enhances the mechanical properties of the material. XG-CoPI10 exhibits good chemical stability with mass retention exceeding 89% in organic solvents. This material also possesses a high mechanical strength of 35.50 MPa under compressive stress. Furthermore, it demonstrates excellent reusability by maintaining 98% of oil sorption capacity after 10 cycles. These properties establish XG-CoPI10 as a promising candidate for practical oil spill remediation and industrial wastewater treatment. Unlike conventional polymer sorbents that suffer from solvent swelling, mechanical degradation, or limited recyclability. The fluorinated polyimine xerogel provides a unique

Table 6 Comparison of oil sorption capacity and mechanical properties of various reported oil adsorbent and this work

Sample	Oil sorption capacity (g g^{-1})	Compression stress at 40% of strain (MPa)	References
Textile waste fibers@PVA	8.0 at 75 °C	0.20	40
Polyimide aerogels@carbon nanotubes	3.6 at 25 °C	4.10	41
	4.2 at 80 °C		
PVDF aerogel	3.5 at 25 °C	0.14	42
XG-CoPI10	3.2 at 30 °C	4.50	This work
	3.8 at 150 °C		

combination of chemical stability, porous structure, and reusability. These attributes are fundamental for successful deployment in practical applications.

The oil sorption capacity and the mechanical properties XG-CoPI in comparison with different xerogel materials are shown in Table 6. The oil sorption capacity of the XG-CoPI10 was observed as 3.2 g g^{-1} at 30 °C. The oil sorption capacity of reported material is higher than XG-CoPI such as textile waste fibers@PVA (8.0 g g^{-1}), Polyimide aerogels@carbon nanotubes (3.6 g g^{-1}). However, the reported materials were not used at very high temperatures. Meanwhile, the XG-CoPI10 exhibited outstanding oil sorption capacity at 150 °C, reaching 3.8 g g^{-1}. Besides that, Xg-CoPI10 shows a better mechanical property compared to another adsorbent. The compression stress at 40% strain reaches 4.50 MPa, significantly higher than PVDF aerogel (0.14 MPa), polyimide aerogel (4.10 MPa). The oil sorption ability and mechanical properties were significantly improved by the low density, porous structure, and intrinsic properties of the XG-CoPI.

4. Conclusion

In summary, this study successfully fabricated a novel and ultralight copolyimine xerogel via a scalable solvent exchange and ambient pressure drying method. The resulting material features a highly porous network with a low density of 0.229 g cm^{-3}. It demonstrates exceptional thermal stability up to 510 °C and chemical resistance, retaining >96% of its initial mass in strong organic solvents like DMF and NMP. Notably, copolyimine xerogel achieves a superior hot vegetable oil adsorption capacity of 3.83 g g^{-1} at 150 °C higher than its ambient-temperature performance (3.21 g g^{-1}). Furthermore, the material maintains high adsorption efficiency across 10 centrifugal desorption cycles. These quantitative findings establish XG-CoPI as a high-performance candidate for high-temperature oil spill remediation and industrial wastewater purification.

Author contributions

Hieu Minh Doan: formal analysis, Ut Thach Dong: formal analysis. Uyen Phuong Trieu: investigation, formal analysis, writing – original draf. Hoan Ngoc Doan: methodology, investigation, writing – review & editing. Vy Tuong Thanh Nguyen: formal analysis, writing – original draf. Trang Thu Thi Nguyen: investigation, formal analysis. Ha Tran Nguyen: formal analysis, writing – review & editing. Phu Phong Vo: funding acquisition, supervision, conceptualization, formal analysis, data curation, visualization, writing – review & editing.

Conflicts of interest

The authors declare that they have no known competing financial interests or personal relationships that could have appeared to influence the work reported in this paper.

Data availability

Data for this article, including Fig. 1–5, Tables 1–5, graphical abstract, and Fig. S1 and S2 are available at figshare at https://doi.org/10.6084/m9.figshare.31293376.

Supplementary information (SI) is available. See DOI: https://doi.org/10.1039/d6ra01173j.

Acknowledgements

References

1 B. Jain, A. K. Singh and M. A. B. H. Susan, *Water Pollution and Remediation: Organic Pollutants*, Springer International Publishing, Cham, 2021, vol. 54.

2 A. Abdulkareem, A. Popelka, P. Sobolčiak, A. Tanvir, M. Ouederni, M. A. AlMaadeed, P. Kasak, S. Adham and I. Krupa, *Materials*, 2021, **14**, 1.

3 S. M. Hailan, I. Krupa and G. McKay, *Int. J. Environ. Sci. Technol.*, 2025, **22**, 3833–3854.

4 B. Zhang, E. J. Matchinski, B. Chen, X. Ye, L. Jing and K. Lee in *World Seas: an Environmental Evaluation*, Elsevier, 2nd edn., 2019, pp. 391–406.

5 K. Sharma, G. Shah, K. Singhal and V. Soni, *Reg. Stud. Mar. Sci.*, 2024, **74**, 103516.

6 A. T. Hoang, X. P. Nguyen, X. Q. Duong and T. T. Huynh, *Environ. Sci. Pollut. Res. Int.*, 2021, **28**, 28876–28910.

7 D. Lang, C. Zhang, Q. Qian, C. Guo, L. Wang, C. Yang, R. Wu, W. Wang, J. Wang and J. Fu, *Cellulose*, 2023, **30**, 7745–7762.

8 G. Mummaleti, F. Kong and J. Agric, *Food Res.*, 2023, **11**, 100506.

9 E. K. Sam, J. Liu and X. Lv, *Ind. Eng. Chem. Res.*, 2021, **60**, 2353–2364.

10 M. Priyanka and M. P. Saravanakumar, *IOP Conf. Ser. Mater. Sci. Eng.*, 2017, **263**, 032018.

11 S. Jiang, S. Agarwal and A. Greiner, *Angew. Chemie - Int. Ed.*, 2017, **56**, 15520–15538.

12 P. R. Aravind, P. Shajesh, G. D. Soraru and K. G. K. Warrier, *J. Sol-Gel Sci. Technol.*, 2010, **54**, 105–117.

13 X. Xie, Z. Zhu, Y. Meng, L. Wang, F. Zhao, L. Chen, L. Jiang, M. Yan and X. Zhou, *Gels*, 2025, **11**, 462.

14 P. Taynton, C. Zhu, S. Loob, R. Shoemaker, J. Pritchard, Y. Jin and W. Zhang, *Polym. Chem.*, 2016, **7**, 7052–7056.

15 R. Hajj, A. Duval, S. Dhers and L. Avérous, *Macromolecules*, 2020, **53**, 3796–3805.

16 M. E. Belowich and J. F. Stoddart, *Chem. Soc. Rev.*, 2012, **41**, 2003.

17 P. Yu, H. Wang, T. Li, G. Wang, Z. Jia, X. Dong, Y. Xu, Q. Ma, D. Zhang, H. Ding and B. Yu, *Adv. Sci.*, 2023, **10**, e2300958.

18 M. Häring and D. D. Díaz, *Chem. Commun.*, 2016, **52**, 13068–13081.

19 S. Taghavi Fardood, F. Yekke Zare, F. Moradnia and A. Ramazani, *J. Rare Earths*, 2025, **43**, 736–742.

20 R. Saha, M. H. Munshi, M. Akter, A. A. R. Shikder and T. Islam, *SPE Polym.*, 2025, **6**, 1–37.

21 D. H. Lee, M. J. Jo, S. W. Han, S. Yu and H. Park, *Polymer*, 2020, **205**, 122879.

22 T. M. Soylu, C. Özel, B. Karakuzu Ikizler, A. C. Özarslan, P. Terzioğlu, Y. B. Elalmis and S. Yücel, *J. Sol-Gel Sci. Technol.*, 2025, **115**, 327–348.

23 E. Raczuk, B. Dmochowska, J. Samaszko-Fiertek and J. Madaj, *Molecules*, 2022, **27**, 787.

24 M. Jafari, Z. Peng, A. Samie, F. Taghavi, A. Khojastehnezhad and M. Siaj, *Molecules*, 2025, **30**, 1–24.

25 D. J. Mulder, L. M. W. Scheres, J. Dong, G. Portale, D. J. Broer and A. P. H. J. Schenning, *Chem. Mater.*, 2017, **29**, 6601–6605.

26 Z. L. Liu, Y. Teng, K. Zhang, Y. Cao and W. P. Pan, *Ranliao Huaxue Xuebao/Journal Fuel Chem. Technol.*, 2013, **41**, 469–476.

27 M. Solà and L. Cavallo, *Chemistry*, 2026, **8**, 7.

28 F. Paquin, J. Rivnay, A. Salleo, N. Stingelin and C. Silva-Acuña, *J. Mater. Chem. C*, 2015, **3**, 10715–10722.

29 J. Debuyck, R. Wink, B. Daelman, R. P. Sijbesma and F. E. Du Prez, *ACS Polym. Au*, 2025, **5**, 613–619.

30 T. Fujita, K. Fuchibe and J. Ichikawa, *Angew. Chemie Int. Ed.*, 2019, **58**, 390–402.

31 C. F. Toncón-Leal, J. Villarroel-Rocha, M. T. P. Silva, T. P. Braga and K. Sapag, *Adsorption*, 2021, **27**, 1109–1122.

32 M. Blachnio, M. Zienkiewicz-Strzalka and A. Derylo-Marczewska, *Int. J. Mol. Sci.*, 2025, **26**, 9255.

33 M. Thommes, *Chemie Ing. Tech.*, 2010, **82**, 1059–1073.

34 L. Tan, Y. Yuan, Z. Zhao, Y. Xu and Y. Yuan, *Int. J. Therm. Sci.*, 2023, **188**, 108226.

35 A. Abdulkareem, A. Popelka, P. Sobolčiak, A. Tanvir, M. Ouederni, M. A. AlMaadeed, P. Kasak, S. Adham and I. Krupa, *Materials*, 2021, **14**, 1086.

36 S. Fuchs, K. Shariati and M. Ma, *Adv. Healthc. Mater.*, 2020, **9**, 1–33.

37 F.-C. Wu, R.-L. Tseng, S.-C. Huang and R.-S. Juang, *Chem. Eng. J.*, 2009, **151**, 1–9.

38 A. A. Sangoremi, *Int. J. Res. Sci. Innov.*, 2025, **XII**, 245–258.

39 X. Chen, X. Fu, Z. Chen, Z. Zhai, H. Miu and P. Tao, *Nanomaterials*, 2025, **15**, 1148.

40 C. Dong, Y. Hu, Y. Zhu, J. Wang, X. Jia, J. Chen and J. Li, *Gels*, 2022, **8**, 684.

41 D. Zhang, Y. Lin, W. Wang, Y. Li and G. Wu, *Appl. Surf. Sci.*, 2021, **543**, 148833.

42 X. Chen, Y. N. Liang, X.-Z. Tang, W. Shen and X. Hu, *Chem. Eng. J.*, 2017, **308**, 18–26.